Journal of Materials Chemistry A

ROYAL SOCIETY OF CHEMISTRY

PAPER

View Article Online
View Journal

Cite this: DOI: 10.1039/d5ta09399f

Supramolecular oscillation-assisted ion transport in solid electrolytes

Yigui Xie,[a] Weiran Zhang,*[a] Luxue Zhang,[a] Xue-Song Liu,[a] Guojian Yang,[b] Yu-Mo Zhang [a] and Sean Xiao-An Zhang *[a]

Solid-state electrolytes are crucial for electrochemical devices, yet the challenge of simultaneously enhancing both ionic conductivity and stability—rather than sacrificing one for the other—remains a critical issue. In this work, a high-performance solid polymer electrolyte (HP-SPE) membrane that successfully integrates exceptional stability with high ionic conductivity was developed. It is based on a polyvinyl butyral (PVB) matrix coupled with (3-glycidyloxypropyl)trimethoxysilane (KH560) and lithium bis(trifluoromethanesulfonyl)imide (LiTFSI), and was fabricated through an ultra-low residual solvent content drying (ULD) process. The high overall performance of HP-SPE was achieved through the binding of trace residual solvents within LiTFSI and the polymer matrix, a mechanism referred to as "supramolecular oscillation-assisted ion transport". HP-SPE achieved an ionic conductivity of 10^{-5} S cm^{-1} at 30 °C (for over two months). The decomposition temperature reached 250 °C, achieving a comprehensive improvement in both conductivity and stability. By applying the HP-SPE membrane to emerging electrochromic devices, these electrochromic devices achieved rapid color switching (3.1 s for coloration and 6.1 s for bleaching), uniform color transition, and steady-state operation without overheating for up to 160 hours, the best results reported to date. This work establishes HP-SPE as a versatile material platform, demonstrating immediate success in electrochromics and revealing significant potential for deployment in next-generation, high-safety solid-state batteries.

Received 19th November 2025
Accepted 6th January 2026

DOI: 10.1039/d5ta09399f

rsc.li/materials-a

Introduction

Energy materials and devices are fundamental and increasingly critical to driving the global energy system towards sustainable and renewable energy sources.[1–3] Electrolytes—whose stability, safety, and rapid response are critical for the performance of energy storage and conversion devices— are essential components in electronic devices and electrochemical energy storage systems.[4–6] Currently, a major research focus is balancing higher energy density and faster response, with the simultaneous goals of ensuring device safety and long-term stability.[7–9] Therefore, there is a pressing need to develop electrolytes with long-term chemical and electrochemical stability, high-temperature resistance, and high ionic conductivity to improve the performance limits of energy devices.

Solid-state electrolytes, including inorganic ceramic solid electrolytes,[10,11] polymer solid electrolytes[12,13] and composite solid electrolytes,[14,15] are seen as the key pathway to achieving compatibility between high safety and high energy density. In particular, all-solid-state polymer electrolytes show great potential in fields such as power batteries[16–19] and smart devices,[20,21] due to their excellent interfacial compatibility, mechanical properties, and processability.[22–25] However, there are often inherent trade-offs between their core performances, such as ionic conductivity, mechanical strength and interfacial stability. Specifically, the rigid polymer backbone needed to achieve high mechanical strength restricts the motion of chain segments, thereby inhibiting ion migration. Conversely, to ensure higher ion conductivity and good interfacial contact, their mechanical properties have to be compromised. In particular, the restriction of chain segment movement and strong Lewis acid–base interactions result in high energy barriers to ion migration.[26,27]

What is more, the presence of trace residual solvents in electrolytes is a critical factor influencing the performance and reliability of all-solid-state energy storage devices. Studies have shown that the existence of residual solvents can greatly enhance ion transport capabilities, while at the same time causing performance instability.[28–30] Therefore, it has long been expected that highly ordered, energetically stable microstructural materials could effectively suppress the disordered migration of conventional solvent molecules and ions, achieving long-term stability from a thermodynamic perspective. This points to a long-standing core challenge in the field, which is how to achieve the "just right" presence of solvents within a very narrow compositional window. This should meet the needs of both avoiding the safety risks and

[a]State Key Laboratory of Supramolecular Structure and Materials, College of Chemistry, Jilin University, Changchun, 130012, P. R. China. E-mail: seanzhang@jlu.edu.cn; zhangweiran@jlu.edu.cn

[b]Smart Materials for Architecture Research Lab Innovation Center of Yangtze River Delta, Zhejiang University, Jiaxing, 314100, P. R. China

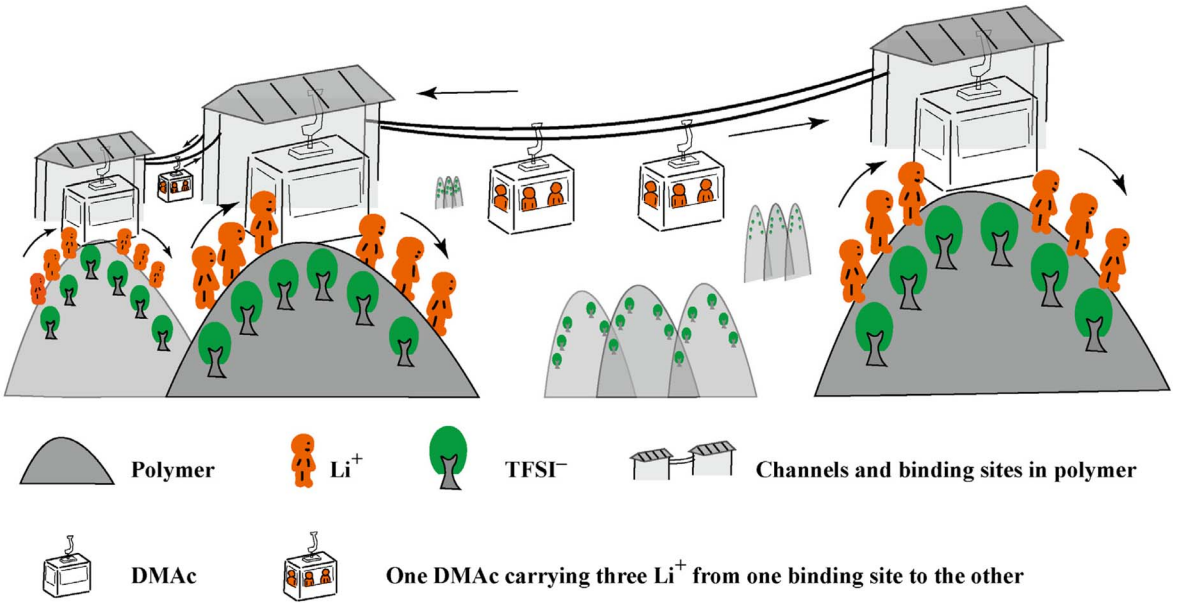

Fig. 1 Schematic of DMAc dynamically assisting Li^+ transport in the polymer electrolyte.

stability issues associated with free residual solvents and serving as a "cable car" for fast ion transport, significantly improving migration rates. Therefore, it is crucial to employ residual solvent molecules in precisely controlled ways to meet the requirements above, thereby yielding solid polymer electrolyte membranes with excellent overall performance. However, there is a lack of systematic understanding of the structure–activity relationships between residual solvent state, content, and transport mechanisms, and furthermore, there is currently a lack of rational design strategies that balance high conductivity and high stability in solid polymer electrolytes.

To address this challenge, we propose a novel solid-state electrolyte design concept: an ion-combined solvent–polymer system in a local coordination environment with a novel "supramolecular oscillation-assisted ion transport" mechanism, which is stable yet retains dynamic migration characteristics, as shown in Fig. 1. A simple and efficient ULD process was employed to successfully obtain a high-performance solid-state polymer electrolyte (HP-SPE) that was in the membrane state, highly adhesive, and possessed excellent overall performance. HP-SPE was investigated to gain mechanistic insights into its high ion conductivity and stability, and was successfully incorporated into an electrochromic device that exhibited outstanding performance. This breakthrough design, centered on utilizing strongly bound residual solvents to assist ion transport, effectively mitigates the long-standing trade-off between conductivity and stability in solid-state electrolytes, thereby opening up new avenues for developing future high-performance, high-safety electronics.

Results and discussion

Through an ultra-low drying (ULD) process, as shown in Fig. 2a, which was a regular vacuum drying treatment (performed at 80 °C for 48 h in a vacuum oven connected to an oil rotary vane pump, with the vacuum level maintained at 133 Pa) and subsequently combined with a convection flow drying treatment (a continuous stream of compressed air, at ambient temperature), a flexible, self-supporting and transparent high-performance solid-state polymer electrolyte film (HP-SPE) was obtained (Fig. 2b). HP-SPE was easy to access, prepare and process. Moreover, the transmittance of HP-SPE over the entire visible region was over 90% (Fig. S1), which ensured its application capabilities in transparent display, optoelectronics, smart glass and other fields. Quantitative ^{1}H NMR analysis using an internal standard (Method S5) confirmed that the residual DMAc content in HP-SPE was 4% (Fig. 2c, S2 and S3). This exceptionally low level represented a state-of-the-art value for the retention of residual solvents in solid-state polymer electrolytes.

To explore the indispensable roles of vacuum drying treatment and convection flow drying treatment in the ULD process of HP-SPE, each method was applied individually. As shown in Fig. S4, both the vacuum and convection drying methods individually produced films that were non-free-standing, highly viscous, and exhibited poor film-forming ability due to excessive residual solvent, which was measured at 14% and 40%, respectively; the corresponding membranes were termed C-14% and C-40%, respectively. The significant difference in residual solvent content indicated that the initial vacuum drying treatment was more effective at removing solvents. The film formation process was kinetically controlled, where the evaporation-induced concentration gradient drove polymer chain reconfiguration. A slow evaporation rate was therefore utilized to promote sufficient chain relaxation, which successfully produced a dense, homogeneous film with minimal defects.[31,32] Residual solvent molecules that did not evaporate promptly became trapped within the polymer matrix and could not be

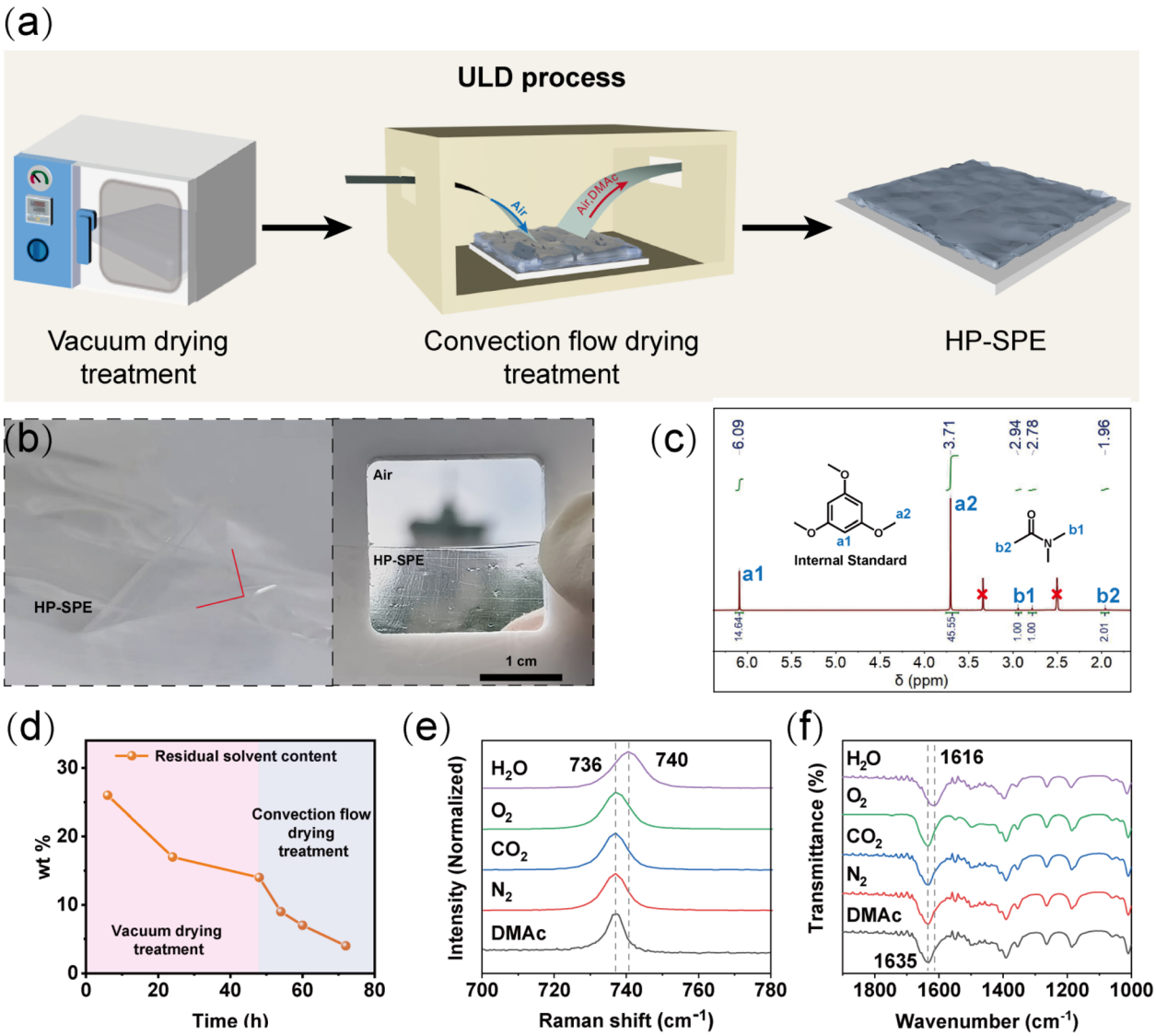

Fig. 2 (a) Schematic diagram of the ULD process. (b) Physical images of HP-SPE showing its self-supporting and transparent properties. (c) ^{1}H NMR (400 MHz, DMSO-d_6) spectra of HP-SPE to detect the residual solvent content using the NMR internal standard method. (d) The residual solvent content of HP-SPE during the ULD process. (e) Raman spectra and (f) FT-IR spectra of DMAc solutions before and after purging by different gas components in the air. Each gas was delivered at a controlled flow rate of 25 mL min^{-1} for 60 minutes, resulting in a total gas volume of 1.5 L per experiment. The black curves represent the spectra of the DMAc solution before gas purging. The red, blue, green, and purple curves corresponded to the spectra after purging nitrogen, carbon dioxide, oxygen, and water vapor, respectively, into the DMAc solution.

readily removed. Thus, the vacuum drying process offered the advantage of rapid film formation, which came at the cost of a high residual solvent content.

In contrast, convection flow drying treatment facilitated solvent evaporation through interaction between air and DMAc molecules, resulting in a comparatively slower process. The convection flow drying process was effective only when applied to a pre-vacuum-dried film, enabling a reduction of residual solvent beyond the capability of either single process. Used in isolation, it produced films with severe phase separation (Fig. S5) and high residual solvent content. The fact that the curve of residual solvent content varied with time during the ULD process (as shown in Fig. 2d) also confirmed this conclusion. The vacuum drying process caused a large amount of solvent to evaporate, reducing it to 14%, while the convection flow drying process further removed the residual solvent content to 4%.

To investigate the binding mechanism between DMAc and flow air, experiments on the individual interaction of each component in the air with DMAc were conducted. As shown in Fig. 2e and f, both Raman and FT-IR spectra proved that O_2, CO_2 and N_2 in the air did not combine with DMAc, resulting in no change to the spectral features of DMAc. However, water vapor would cause the peak position to shift (from 736 cm^{-1} to 740 cm^{-1} and from 1635 cm^{-1} to 1616 cm^{-1}, respectively), which indicated that it was water vapor that interacted with DMAc in the air. Due to the strong affinity between water vapor and DMAc molecules, flowing air could co-evaporate them from

the film. In this process, water vapor acted as a carrier, entraining DMAc molecules into the air stream and thus drastically lowering the overall residue solvent content of the system. Subsequently, to better simulate the high concentration environment of LiTFSI in the polymer, the DMAc solution was replaced with a solution where the mass ratio of DMAc to LiTFSI was 20 : 1, and the same gas experiment was conducted. As shown in Fig. S6, consistent with the previous phenomenon, only water vapor could affect the peak position of DMAc. However, the influence on the peak position was significantly weaker, which implied a preferential and stronger binding of LiTFSI to DMAc over water. The ULD process presented a viable strategy for fabricating solid-state membranes with ultra-low solvent residue.

These data strongly demonstrated the advanced and superior nature of the ULD method, which involved sequential vacuum drying treatment and convection flow drying treatment. The primary step rapidly formed the film, while the secondary step focused on extensively removing the solvent. Each step served a distinct function, making the sequence critical. This innovative method, together with a mechanistic study of the process, provided a solid theoretical foundation for addressing the challenges of solvent removal. ULD is a simple and efficient processing method, which provides a promising strategy for the

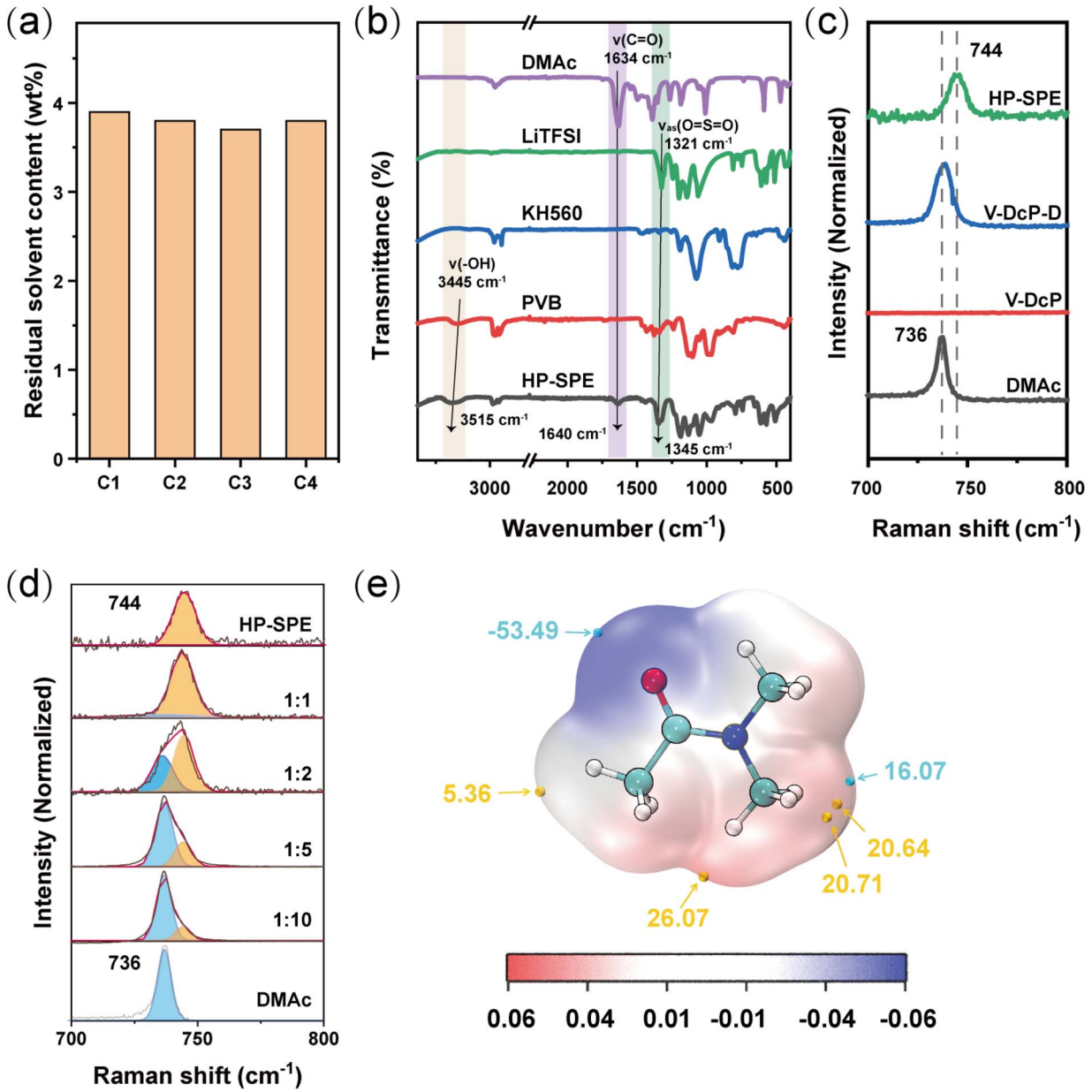

Fig. 3 (a) Comparison of the residual solvent content of HP-SPE after treatment under different harsh conditions with the initial ones; C1, C2, C3, and C4 represent the initial state, treatment at 100 °C and 10 MPa for ten hours, freezing in liquid nitrogen for ten hours, and being left for half a month under ambient conditions, respectively. (b) FT-IR spectra of HP-SPE and all raw materials. (c) Raman spectra of DMAc, V-DcP, V-DcP-D and HP-SPE. (d) Raman spectra of DMAc, HP-SPE and different weight ratios of LiTFSI to DMAc. (e) DMAc surface electrostatic potential calculation.

rapid and efficient removal of solvent to produce high-quality polymer films, demonstrating broad applicability for diverse solvent-processing fields.

To test the stability of HP-SPE, the material was exposed to harsh environmental conditions. As shown in Fig. 3a, the residual solvent content of HP-SPE remained largely unchanged after treatment, regardless of how harsh the environment was, indicating that HP-SPE avoids drawbacks such as volatilization and aggregation observed with free solvents. This outstanding performance provides a foundation for commercial usage under extreme conditions. The FT-IR spectra (Fig. 3b) of HP-SPE and its individual components reveal critical interactions through distinct peak shifts. Compared to pure PVB, the O–H stretching vibration in HP-SPE shifts from 3445 to 3515 cm^{-1}, indicating restructuring of the hydrogen-bonding network.[33] Compared to pure DMAc solution, the C=O stretch of incorporated DMAc appears at 1640 cm^{-1}, confirming strong C=O···Li^+ coordination.[34] Importantly, the O=S=O asymmetric stretch of LiTFSI exhibits a pronounced 24 cm^{-1} blue-shift (from 1321 to 1345 cm^{-1}) in the composite, providing direct evidence for significant ion-pair dissociation.[12] These collective shifts corroborate the formation of a unique interacting microenvironment that stabilizes the components and promotes Li^+ mobility. The ultra-low amount of solvent remaining in the HP-SPE membrane was tightly bound to some component in the membrane; thus, it could not be "driven away" from the membrane by air. The membrane consisted of a cross-linked PVB skeletal framework acting as the matrix, and LiTFSI as the electrolyte. To identify which component in the membrane tightly binds with DMAc, DMAc was mixed with each of the two components separately. For the solution of DMAc combined with cross-linked PVB (DcP), after vacuum drying treatment (V-DcP), no residual solvent content was detected (Fig. S7), and a dry membrane was obtained (Fig. S8a). However, for the solution of DMAc combined with LiTFSI (DcLi), after vacuum drying treatment (V-DcLi), it maintained its liquid solution form instead of becoming a dry powder (Fig. S8b), indicating a strong binding effect between LiTFSI and DMAc. V-DcP was applied with a small layer of DMAc residual solvent (V-DcP-D) to test the free state of DMAc in the membrane. The FT-IR spectra of V-DcP and V-DcP-D were compared (Fig. S9), and the data showed that V-DcP-D had distinct DMAC peaks while V-DcP did not. Obviously, the residual DMAc in the membrane was tightly bound with LiTFSI. Moreover, the distinct contrast observed in the AFM topography of HP-SPE *versus* V-DcP (Fig. S10) indicates a change in polymer morphology induced by the addition of LiTFSI.

To further investigate the interaction between DMAc and LiTFSI, a comparative analysis of the Raman spectra of HP-SPE, V-DcP, V-DcP-D and DMAc was conducted. As shown in Fig. 3c, the Raman peak of the DMAc solution and V-DcP-D appeared as a single peak at 736 cm^{-1}, while V-DcP showed no absorption at 700–800 cm^{-1}. The Raman spectrum of HP-SPE showed a peak at 744 cm^{-1} and no peak at 736 cm^{-1}, which proved that the form of DMAc in HP-SPE was different from the free state in the solution, resulting in an 8 cm^{-1} shift. To determine whether this 8 cm^{-1} shift was caused by the binding of LiTFSI and DMAc, solutions of LiTFSI dissolved in DMAc at different mass ratios were prepared, and Raman spectra of this series of solutions were obtained. As shown in Fig. 3d, the curves from bottom to top correspond to the decreasing proportion of DMAc and the increasing proportion of LiTFSI. In the Raman spectra, a dominant peak at 736 cm^{-1} and a minor shoulder at 744 cm^{-1} were observed under high DMAc content. As the DMAc/LiTFSI ratio decreased, the intensity of the peak at 736 cm^{-1} progressively diminished and almost vanished, whereas the signal at 744 cm^{-1} intensified accordingly. Through comparative analysis of the Raman spectra of membranes fabricated with varying compositions, as well as solutions with different DMAc-to-LiTFSI ratios, it was demonstrated that the Raman peak at approximately 736 cm^{-1} corresponded to free DMAc, while the peak near 744 cm^{-1} was associated with DMAc-LiTFSI complexes. The absence of the free solvent peak in the NMR or optical spectrum indicated that virtually all DMAc molecules were coordinated with Li^+ ions, which strongly confirmed the absence of free DMAc residues. This molecular environment provided a robust foundation for the long-term stability of HP-SPE. The mode of combination of DMAc and LiTFSI was key to exploring the microscopic processes. Based on the mass of each component, the molar ratio of LiTFSI to DMAc was calculated to be 3 : 1 (Note S1). Calculations of the surface electrostatic potential[35] provided direct evidence for strong binding sites between LiTFSI and DMAc molecules (Fig. 3e), supporting the notion that DMAc existed primarily in a bound state within the system.

This binding pattern ensured that LiTFSI migration was not solely governed by polymer chain dynamics but was efficiently facilitated by the ordered, dynamic motion of the residual solvents. This process, which we term "supramolecular oscillation-assisted ion transport", not only accelerated lithium-ion conduction but also, in contrast to solvent-rich quasi-solid-state electrolytes, guaranteed the stable retention of the solvent within the system. The combination of ultra-stability and fast kinetics offered by this mechanism was key to the outstanding device performance.

To further evaluate the comprehensive properties of HP-SPE, its thermal stability, conductivity and electrical stability were tested. TGA tests on V-DcP-D, residual solvent content of about 26% of the membrane (C-26%), residual solvent content of about 17% of the membrane (C-17%) and HP-SPE were conducted. As shown in Fig. 4a and S11, a strong correlation was observed, with the decomposition temperature of the membrane increasing as the free solvent content decreased. It was found that V-DcP-D began to decompose at 100 °C, and the C-26% and C-17% membranes both began to decompose before 150 °C. Excitingly, HP-SPE began to decompose at a temperature as high as 250 °C, which was much higher than those of the other three membranes containing free residual solvents, further confirming the stable existence of DMAc in HP-SPE. Notably, 250 °C is the threshold, marking the onset of explosive thermal runaway,[36] demonstrating that HP-SPE complies with the safety temperature for thermal runaway, and this performance is outstanding in the field of electrochemistry.

Subsequently, the impedance of the membrane was measured at various temperatures. The impedance data were fitted using an equivalent circuit model ($R_1 + [R_2 \| CPE_1] + CPE_2$),

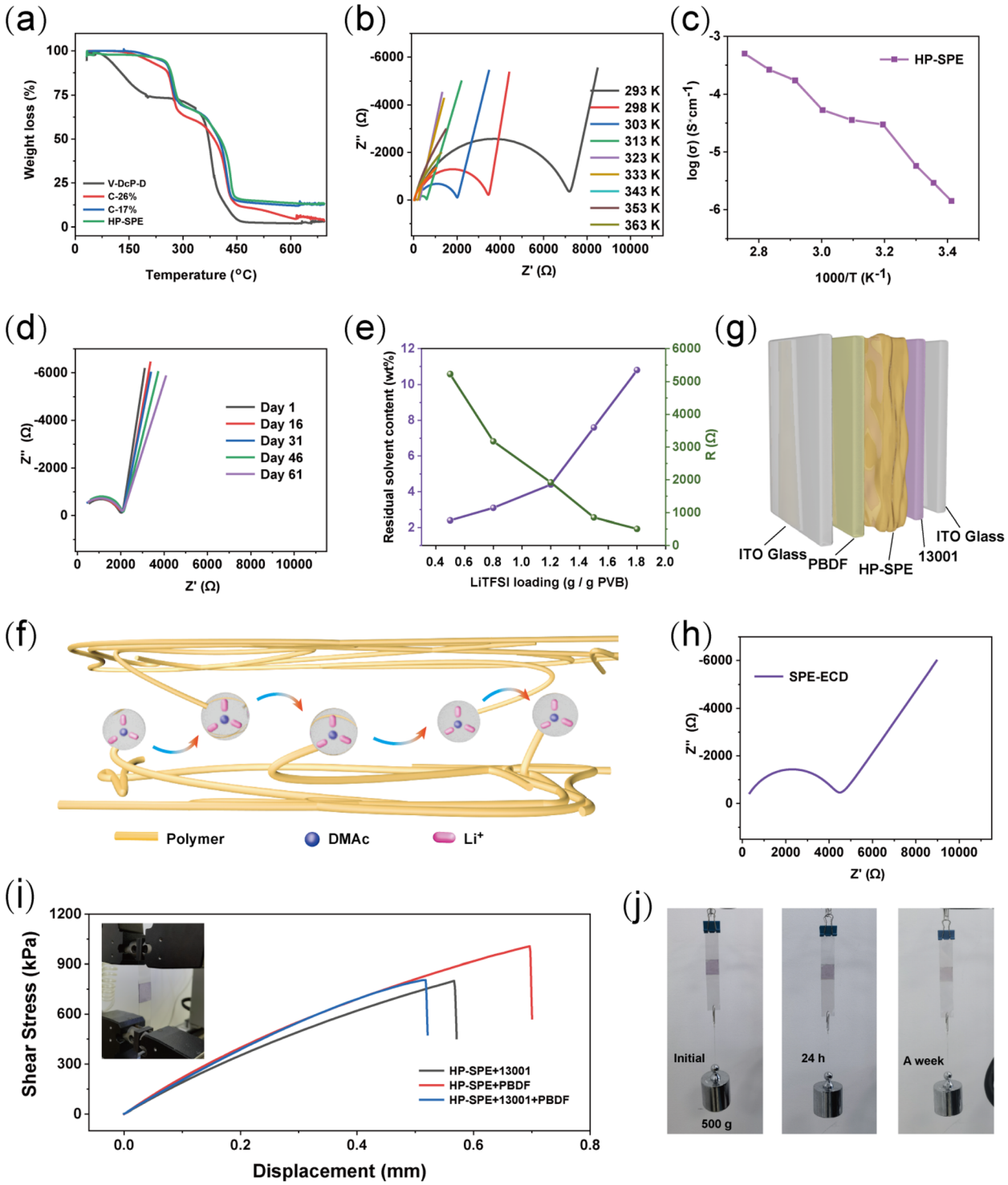

Fig. 4 (a) TGA curves of HP-SPE and contrast membranes. (b) Impedance spectra of HP-SPE under variable temperatures. All Nyquist plots are presented on the same scale for direct comparison in the paper. (c) The variation in the ionic conductivity of HP-SPE with temperature. (d) Successive Nyquist plots (15 days intervals) of HP-SPE over 2 months of storage. The near-perfect overlap of the semicircular segments demonstrates the stability of the bulk resistance. (e) Correlation between LiTFSI loading, residual solvent content (left axis), and bulk resistance at 30 °C (right axis). The optimal loading (~1.2 g) is indicated. (f) The transport mechanism of LiTFSI in polymers. (g) A structural schematic diagram of SPE-ECD. (h) Impedance of SPE-ECD at room temperature. (i) Mechanical property testing of SPE-ECD and comparison devices. (j) Load-bearing test of SPE-ECD.

where R_1 represents the ohmic series resistance, and R_2 corresponds to the bulk electrolyte resistance used for conductivity calculation. The full fitting parameters and detailed element definitions are provided in Fig. S12. As depicted in Fig. 4b, the resistance exhibited continuous decrease with increasing temperature. The temperature dependence of the ionic

conductivity is summarized in Fig. 4c. HP-SPE demonstrated an ionic conductivity of 5.0×10^{-6} S cm^{-1} at 30 °C, indicating favorable ion transport properties. This further confirmed that the bonded DMAc significantly enhanced the migration speed of LiTFSI. Furthermore, HP-SPE showed notable long-term stability. Impedance measurements conducted at 30 °C revealed consistent values over a period of two months, as illustrated in Fig. 4d. This result demonstrated the high stability of LiTFSI-bound DMAc within the system, without exhibiting the inherent disadvantages of free solvents.

To rationalize the LiTFSI concentration (1.2 g per 1 g PVB) employed throughout this work, its effect was systematically investigated. As shown in Fig. 4e and S13, the residual DMAc content and the bulk ionic resistance exhibit opposing trends with salt loading, confirming that 1.2 g represents an optimal balance between achieving high ionic conductivity and maintaining material stability. Furthermore, the transport mechanism of LiTFSI bonded with DMAc within the polymer was illustrated. The anions are strongly anchored to the polymer sites, while the cations undergo dynamic movement within the system, facilitated by DMAc molecules. This transport mechanism strikes a balance between the restricted mobility characteristic of pure polymer electrolytes and the excessive fluidity prevalent in well-solvated systems. These large clusters facilitate chain-like ion transport through a binding-release mechanism in the polymer, as depicted in Fig. 4f. With the assistance of residual solvents, LiTFSI can propagate more rapidly within the system. Thus, even in a self-supporting solid-state form, the electrolyte still exhibits excellent conductivity, further highlighting the superiority of HP-SPE.

Electrochromic devices (ECDs) hold promise for smart windows and wearable electronics, but face commercialization hurdles like limited durability and high residual solvent content.[37–42] Solid polymer electrolytes (SPEs) offer a solution with high ionic conductivity and minimal residual solvents, directly addressing these stability issues.[43,44] Thus, a sandwich-structured electrochromic device based on HP-SPE (SPE-ECD) was fabricated, as shown in Fig. 4g, using an HP-SPE membrane as the conductive layer, a polythiophene-based electrochromic molecule (13 001) as the electrochromic layer, poly (benzodifurandione) (PBDF) as the counter layer, and ITO glass as the transparent electrode. As characterized by NMR (Fig. S14 and S15), neither the electrochromic layer nor the counter layer contained solvents, confirming that both the counter layer and the electrochromic layer in SPE-ECD were entirely solid-state. The ion-conducting layer contained only trace amounts of bonded DMAc, rather than being free. As a result, the residual solvent content in the entire device was extremely low, making SPE-ECD effectively an all-solid-state device. The impedance of SPE-ECD was tested at room temperature, and a conductivity of 2.0×10^{-6} S cm^{-1} was calculated (Fig. 4h), demonstrating that HP-SPE maintained excellent conductive capability even when integrated into an electrochemical device. The high ionic conductivity of the device was attributed to the dynamic transport of lithium ions facilitated by the DMAc in HP-SPE, ensuring fast ion mobility.

Effective interfacial contact plays a critical role in all-solid-state devices by significantly reducing contact resistance, which necessitates the measurement of interfacial shear strength. The test results of HP-SPE *versus* other layers, shown in Fig. 4i, revealed that the shear strength between the HP-SPE membrane and the 13 001 layer was approximately 800 kPa (black line), while that between the HP-SPE membrane and the PBDF layer was about 1000 kPa (red line), indicating significantly stronger adhesion with the PBDF layer. This suggested that the adhesion performance of the device was determined primarily by the interface between the HP-SPE membrane and the 13 001 layer. Further testing of a three-layer (13001/HP-SPE/PBDF) device yielded a shear strength of around 800 kPa (blue line), consistent with the two-layer test results. A shear strength of 800 kPa sufficiently demonstrated excellent adhesion between the membrane and the other layers, due to the abundant hydroxyl groups in the PVB structure, enabling powerful interfacial adhesion.[34] This superior stability can be directly attributed to the intrinsic molecular properties of the selected PVB polymer, thereby laying a solid foundation for the enhanced stability of SPE-ECD. A load-bearing test demonstrated that SPE-ECD could support a 500 g weight for one week without any signs of detachment, as shown in Fig. 4j, further confirming excellent adhesion between the PVB layer and the other functional layers. Additionally, the strong adhesive properties of PVB ensured that the contact resistance between HP-SPE and the two adjacent layers remained low, which was essential for the long-term stability and uniform coloration of the device.

Comprehensive tests on the electrochromic performance of SPE-ECDs were conducted. As shown in Fig. 5a, SPE-ECD exhibited reversible coloration and bleaching under low-voltage stimulation, with a transmittance change of 25%. The maximum current density of SPE-ECD reached 0.06 mA cm^{-2} (Fig. S16), demonstrating its excellent conductivity. As illustrated in Fig. 5b, a transmittance change of 7% was achieved under a voltage stimulus of +0.1 V for 5 s. The transmittance change increased with higher voltages, reaching 23% at +0.8 V. Beyond this voltage, no significant further change in transmittance was observed despite increasing voltage. Therefore, +0.1 V was selected as the turn-on voltage and +0.8 V as the working voltage. The optical modulation (ΔT) was 24.9% after stimulation of +0.8 V for 5 s. The response times of SPE-ECD were 3.1 s and 6.1 s for bleaching and coloring, respectively (Fig. 5c), indicating the rapid ion conduction capability of SPE-ECD, which was attributed to its unique ion transport mechanism. The optical switching performance of this device showed 10% attenuation after 1500 "bleaching–coloring" cycles, as illustrated in Fig. 5d, confirming the exceptional cycling stability of the device, which further proved that HP-SPE was ultra-stable and fast-conducting. In HP-SPE, combined residual solvent molecules play the role of "cable cars", assisting ions in inter-chain hopping under the control of an electric field, significantly improving ion migration. At the same time, due to their strong binding state, these combined residual solvent molecules are less likely to dissociate, volatilize, or aggregate,

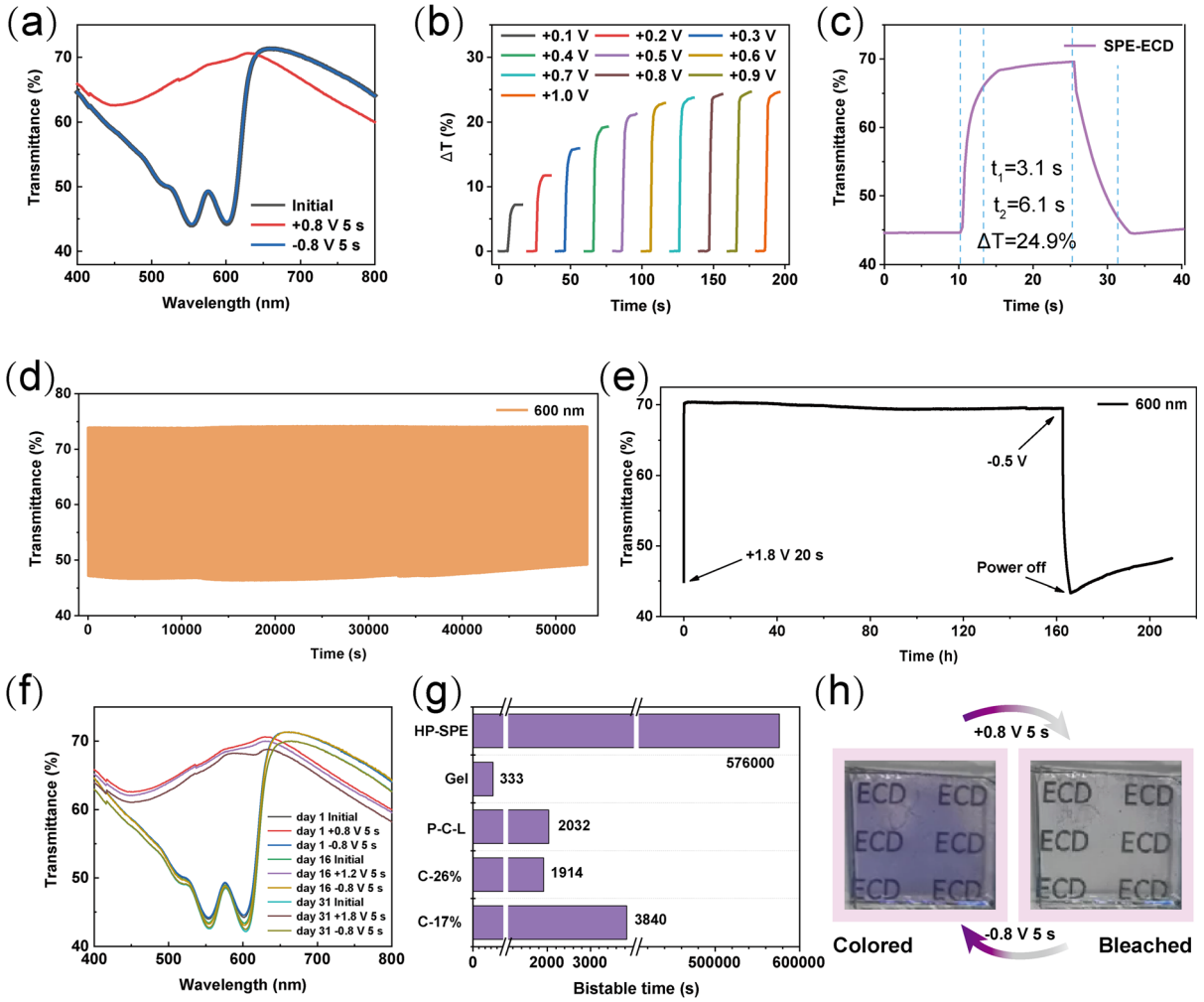

Fig. 5 (a) Transmittance spectra of SPE-ECD without stimulation, at +0.8 V for 5 s and at −0.8 V for 5 s. (b) Comparison of changes in transmittance spectra of SPE-ECD at 600 nm under different voltages for 5 s. (c) The transmittance at 600 nm of SPE-ECD under voltages of +0.8 V, 5 s/OCV, 10 s/−0.8 V, 5 s/OCV. t1 and t2 refer to the bleaching time and coloring time, respectively. (d) The cycling stability of SPE-ECD at 600 nm, under voltages of +0.8 V, 5 s/OCV, 10 s/−0.65 V, 7.5 s/OCV, 10 s. (e) Changes in transmittance at 600 nm of SPE-ECD under voltages of +1.8 V, 20 s/OCV, 160 h/−0.5 V 0.5 h/OCV. (f) Transmittance spectra of SPE-ECD on different storage days. (g) Optical memory time (from the highest ΔT to 90% of the highest ΔT) of SPE-ECD and the contrast devices. (h) Physical photographs of the device showing a reversible color change under low-voltage stimulation.

achieving a significant enhancement in ionic conductivity while maintaining high stability.

The optical stability of SPE-ECD was assessed, as shown in Fig. 5e. Initially, in the colored state, the device remained stable. After applying a +1.8 V voltage for 20 s, the device transitioned to a colorless transparent state, which remained stable for 160 hours with only a 4% decrease in ΔT. A small voltage of −0.5 V was then applied, and after prolonged stimulation, the device returned to its original state. Due to multiple intermediate states in polythiophene, a slow spectral rebound occurred after removal of the voltage, but it eventually stabilized near the initial state. The 160 hours stability of the device demonstrated the excellent performance of the solid-state electrolyte, avoiding the drawbacks of free solvents that could compromise performance. The excellent cyclic stability and rapid switching kinetics of the device can be attributed, in part, to efficient ion transport within the solid-state configuration. This is underpinned by a high apparent Li^+ transference number of ~0.998 (Fig. S17 and Table S1). This value indicates both that charge transport is dominated by Li^+ ions and that $TFSI^-$ anions are effectively immobilized within the matrix, as conceptually depicted in Fig. 1. Consequently, polarization losses from counter-ion accumulation are minimized, ensuring consistent performance. Durability tests over one month showed no significant change in ΔT (Fig. 5f), further confirming the outstanding stability of the device. The exceptional stability of SPE-ECD was attributed to the extremely low residual solvent content in HP-SPE. In this system, the residual solvent was bound with LiTFSI and remained stably integrated, preventing the presence of free solvent that could have caused detrimental effects and defects in the device. As a result, the stability of the

device was greatly enhanced, as evidenced by its significantly prolonged bistable duration and improved durability.

To further investigate the impact of ultra-low residual solvent content on bistable time, devices were prepared with gel layers containing PC and PMMA (gel film), as well as photo-crosslinked PEGDA and PC (P-C-L film), with residual solvent content of 26% (C-26% film) and with residual solvent content of 17% (C-17% film), as the ion transport layer. For consistency, the electrochromic layer and the counter layer remained the same. By comparing the time it took for SPE-ECD and the other four contrast devices to drop from the highest point to 90% of the highest ΔT, it could be seen that SPE-ECD had an ultra-long memory effect (>160 h), which was 1730 times that of the gel device (333 s), 283 times that of the photocrosslinked device (2032 s), 301 times that of the C-26% device (1914 s) and 165 times that of the C-17% device (3840 s), as shown in Fig. 5g, S18 and Table S2. This also reflects the fact that the lower the solvent residue, the better the device stability, and the ultra-low residual solvent condition provided a stable environment for both the bleaching and coloring states of the electrochromic molecules.

The above experimental results showed that HP-SPE enabled ultra-stable and fast ion transport. When a voltage was applied, under the influence of the electric field, DMAc molecules carried LiTFSI through supramolecular interactions, facilitating extremely rapid transport within the system and ensuring excellent conductivity. In the absence of an applied voltage, there were no free liquids in the system, allowing the other components to remain stable without being affected by issues such as liquid evaporation or aggregation, ensuring the overall stability of the device. The supramolecular ion transport mechanism of HP-SPE achieved both high conductivity and stability, representing a breakthrough in electrochemical devices. This also provides valuable insights for addressing solvent-related issues in other fields of research. Finally, a 1 cm $\times$ 1 cm device was fabricated and placed on paper with the letters "ECD". The text remained clearly visible, and a distinct color change was observed before and after voltage application (Fig. 5h). Moreover, the device exhibited highly uniform coloration, attributable to the excellent adhesion of HP-SPE. A comparison of the ionic conductivity and electrochromic performance between SPE-ECD and previously reported devices based on various electrolytes is summarized in Table S3. The data highlight the superior overall performance of SPE-ECD. The supramolecular oscillation-assisted ion transport mechanism is key to the concurrent high ionic conductivity and outstanding stability of our solid electrolyte. The resultant electrochromic device achieves a superior combination of ultra-stability and fast ion transport, paving the way for its viable commercialization. In addition to its excellent electrochromic performance, the ionic conductivity of HP-SPE also makes its application in the field of solid-state batteries possible. Preliminary battery tests (Fig. S19) indicate that it has good ion transport capability as a solid-state electrolyte (critical current density $\sim$2.84 mA cm^{-2}), although further optimization of material and interface engineering is still needed for long-term cycling. This attempt preliminarily confirms the potential of this material for multifunctional applications and lays a foundation for subsequent interdisciplinary research.

Conclusions

This work developed a novel ULD method for efficient solvent removal, enabling the fabrication of a solid-state polymer electrolyte membrane HP-SPE with exceptional comprehensive properties. The obtained membrane demonstrates remarkable performance, including thermal stability up to 250 °C, long-term durability, high ionic conductivity and excellent mechanical robustness. Through multiple characterization techniques, this excellent performance was verified to be attributed to the strong binding between DMAc and LiTFSI within the system, a finding that led us to propose the new conceptual mechanism of "supramolecular oscillation-assisted ion transport". When applied in all-solid-state electrochromic devices, HP-SPE afforded outstanding operational stability. Beyond electrochromics, HP-SPE presents a versatile platform for next-generation solid-state batteries. Its exceptional interfacial stability and high Li^+ transference number address critical challenges in battery systems, making the exploration of its performance in lithium-metal batteries a compelling next frontier.

Author contributions

Y. X., Y.-M.Z. and S. X.-A. Z. conceived and design this project. Y. X. and L. Z. conducted the experiments. X.-S. L. synthesized the materials. G. Y. provided the technical support. Y. X., W. Z. and L. Z. researched the mechanism and fabricated the devices. Y. X., W. Z. and S. X.-A. Z. conducted the analysis and wrote the manuscript. The project was directed and supervised by S. X.-A. Z., Y.-M. Z. and W. Z.; all authors have given approval to the final version of the manuscript.

Conflicts of interest

There are no conflicts to declare.

Data availability

The data supporting this article have been included as part of the supplementary information (SI). Supplementary information: Fig. S1–S19, Tables S1–S3, Methods S1–S6 and Note S1. See DOI: https://doi.org/10.1039/d5ta09399f.

Acknowledgements

This study was supported by the National Natural Science Foundation of China (Grant No. 22475079), the Jilin University Interdisciplinary Youth Innovation Team (Grant No. 45123031C002), and the Fundamental Research Funds for the Central Universities.

References

1 S. G. Yoon, B. S. Vishnugopi, D. L. Nelson, A. X. B. Yong, Y. Wang, S. E. Sandoval, T. A. Thomas, K. A. Cavallaro, P. Shevchenko, E. P. Alsaç, C. Wang, A. Singla, J. R. Greer, E. Ertekin, P. P. Mukherjee and M. T. McDowell, *Science*, 2025, **388**, 1062.
2 J. Min, S.-M. Bak, Y. Zhang, M. Yuan, N. F. Pietra, J. A. Russell, Z. Deng, D. Xia, L. Tao, Y. Du, H. Xiong, L. Li, L. A. Madsen and F. Lin, *Nat. Nanotechnol.*, 2025, **20**, 787.
3 Y. Chen, T. Xue, C. Chen, S. Jang, P. V. Braun, J. Cheng and C. M. Evans, *Nat. Mater.*, 2024, **23**, 1539.
4 S. Kondou, M. Abdullah, I. Popov, M. L. Martins, L. A. O'Dell, H. Ueda, F. Makhlooghiazad, A. Nakanishi, T. Sudoh, K. Ueno, M. Watanabe, P. Howlett, H. Zhang, M. Armand, A. P. Sokolov, M. Forsyth and F. Chen, *J. Am. Chem. Soc.*, 2024, **146**, 33169.
5 C. Zhong, Y. Deng, W. Hu, J. Qiao, L. Zhang and J. Zhang, *Chem. Soc. Rev.*, 2015, **44**, 7484.
6 T. Ma, B. Fu, H. Feng, Y. Li, Y. Zhai, Y. Tian, Z. Li and Z. M. Su, *Angew. Chem., Int. Ed.*, 2025, **64**, e202501412.
7 Y. Ou, C. Li, H. Zhou, P. Zhou, S. Yan, W. Hou, Y. Lu, X. Ma, Y. Wu, S. Wu, Z. Liu, X. Chen, Y. Xia, W. Zhang, Q. Cao, H. Liu, F. Liu, X. Song, H. Zhou, X. Peng, J. Feng, K. Li, L. Wei, C. Sun, J. Zhang, J. Chen and K. Liu, *CCS Chem.*, 2025, **7**, 2864.
8 X. Zhang, S. Wang, C. Xue, C. Xin, Y. Lin, Y. Shen, L. Li and C. W. Nan, *Adv. Mater.*, 2019, **31**, 1806082.
9 J. Zhu, S. He, H. Tian, Y. Hu, C. Xin, X. Xie, L. Zhang, J. Gao, S. M. Hao, W. Zhou and L. Zhang, *Adv. Funct. Mater.*, 2023, **33**, 2301165.
10 T. Zhang, X. Mu, Y. Li, S. Cong, S. Zheng, R. Huang, F. Geng and Z. Zhao, *Adv. Mater.*, 2024, **36**, 2402670.
11 F. Han, J. Yue, C. Chen, N. Zhao, X. Fan, Z. Ma, T. Gao, F. Wang, X. Guo and C. Wang, *Joule*, 2018, **2**, 497.
12 X. Wang, Y. Yang, Q. Jin, Q. Lou, Q. Hu, Z. Xie and W. Song, *Adv. Funct. Mater.*, 2023, **33**, 2214417.
13 X. Wu, Z. Bai, B. Bao, Q. Zhang, W. Jiang, Y. Li, C. Hou, K. Li and H. Wang, *Adv. Funct. Mater.*, 2024, **34**, 2312358.
14 X. Wang, H. Zhai, B. Qie, Q. Cheng, A. Li, J. Borovilas, B. Xu, C. Shi, T. Jin, X. Liao, Y. Li, X. He, S. Du, Y. Fu, M. Dontigny, K. Zaghib and Y. Yang, *Nano Energy*, 2019, **60**, 205.
15 C.-D. Fang, Y. Huang, Y.-F. Sun, P.-F. Sun, K. Li, S.-Y. Yao, M.-Y. Zhang, W.-H. Fang and J.-J. Chen, *Nat. Commun.*, 2024, **15**, 6781.
16 R. Xu, S. Xu, X. Zhang, Y. Wang, T. Yu, R. Xiao, S. Bai, Z. Sun and F. Li, *Adv. Mater.*, 2025, e13365.
17 K. Zhang, F. Wu, X. Wang, S. Weng, X. Yang, H. Zhao, R. Guo, Y. Sun, W. Zhao, T. Song, X. Wang, Y. Bai and C. Wu, *Adv. Energy Mater.*, 2022, **12**, 2200368.
18 H. Xu, Q. Zhu, Y. Zhao, Z. Du, B. Li and S. Yang, *Adv. Mater.*, 2023, **35**, 2212111.
19 Q. Zhou, J. Ma, S. Dong, X. Li and G. Cui, *Adv. Mater.*, 2019, **31**, 1902029.
20 Z. Shao, A. Huang, C. Ming, J. Bell, P. Yu, Y.-Y. Sun, L. Jin, L. Ma, H. Luo, P. Jin and X. Cao, *Nat. Electron.*, 2022, **5**, 45.
21 J. Zhou, C. Wang, X. Zhang, J. Luo, J. Ji, Y. Wu and S. Tan, *Ind. Eng. Chem. Res.*, 2021, **60**, 17083.
22 Z. Li, J. Fu, X. Zhou, S. Gui, L. Wei, H. Yang, H. Li and X. Guo, *Adv. Sci.*, 2023, **10**, 2201718.
23 W. Li, Y. Zhai, S. Gong, Y. Zhou, Q. Xia, J. Wu and X. Zhang, *Nano-Micro Lett.*, 2025, **17**, 306.
24 R. Chen, Q. Li, X. Yu, L. Chen and H. Li, *Chem. Rev.*, 2019, **120**, 6820.
25 M. B. Dixit, W. Zaman, N. Hortance, S. Vujic, B. Harkey, F. Shen, W.-Y. Tsai, V. De Andrade, X. C. Chen, N. Balke and K. B. Hatzell, *Joule*, 2020, **4**, 207.
26 H. V. Babu, B. Srinivas and K. Muralidharan, *Polymer*, 2015, **75**, 10.
27 E. Cznotka, S. Jeschke, M. Grünebaum and H.-D. Wiemhöfer, *Solid State Ionics*, 2016, **292**, 45.
28 P. Li, J. Hao, S. He, Z. Chang, X. Li, R. Wang, W. Ma, J. Wang, Y. Lu, H. Li, L. Zhang and W. Zhou, *Nat. Commun.*, 2025, **16**, 3727.
29 C. Wang, Z. Wen, W. Chen, J. Cao, X. Wang, F. Zhou, K. Wu, B. Li and Q. Liu, *ChemSusChem*, 2025, **18**, e202500445.
30 J. Shi, T. Koketsu, Z. Zhu, M. Yang, L. Sui, J. Liu, M. Tang, Z. Deng, M. Liao, J. Xiang, Y. Shen, L. Qie, Y. Huang, P. Strasser and J. Ma, *Nat. Mater.*, 2024, **23**, 1686.
31 M. Sônego, L. C. Costa and J. D. Ambrósio, *Polym. Eng. Sci.*, 2016, **56**, 971.
32 Y. Yabuuchi, Y. Minowa, S. Nagamatsu, A. Fujii and M. Ozaki, *ACS Mater. Lett.*, 2021, **4**, 205.
33 T. Chen, H. Wang, Y. Yu, Q. Yan, Z. Wang, J. Yang, L. Li and K. Cui, *Polym. Degrad. Stab.*, 2025, **239**, 111373.
34 N. Kotov, V. Raus and J. Dybal, *J. Phys. Chem. B*, 2018, **122**, 8921.
35 A. Oliver, C. A. Hunter, R. Prohens and J. L. Rosselló, *J. Comput. Chem.*, 2018, **39**, 2371.
36 X. Feng, M. Ouyang, X. Liu, L. Lu, Y. Xia and X. He, *Energy Storage Mater.*, 2018, **10**, 246.
37 Z. Mei, Y. Ding, M. Wang, P. S. Lee, A. Pawlicka, L. Zhao and X. Diao, *Adv. Mater.*, 2025, **37**, 2420578.
38 Y. Xie, W. Zhang, J. Gao, Z. Yao, Y. Yan, X. Zou, G. Yang, Y.-M. Zhang and S. X.-A. Zhang, *Chem. Eng. J.*, 2025, **504**, 158818.
39 I. Song, L. You, K. Chen, W. J. Lee and J. Mei, *Adv. Mater.*, 2024, **36**, 2307057.
40 D. Chen, Z. Tong, Q. Rao, X. Liu, H. Meng and W. Huang, *Nat. Commun.*, 2024, **15**, 8457.
41 Z. Huang, Y. Peng, J. Zhao, S. Zhang, P. Qi, X. Qu, F. Yan, B. Ding, Y. Xuan and X. Zhang, *Nano-Micro Lett.*, 2024, **17**, 98.
42 W. Zhang, Y. M. Zhang, F. Xie, X. Jin, J. Li, G. Yang, C. Gu, Y. Wang and S. X. A. Zhang, *Adv. Mater.*, 2020, **32**, 2003121.
43 Z. Li, J. Fu, X. Zhou, S. Gui, L. Wei, H. Yang, H. Li and X. Guo, *Adv. Sci.*, 2023, **10**, 2201718.
44 P. Ding, Z. Lin, X. Guo, L. Wu, Y. Wang, H. Guo, L. Li and H. Yu, *Mater. Today*, 2021, **51**, 449.

